

# Quenching of galaxies at cosmic noon

## Understanding the effect of environment

Akriti Singh,<sup>1,2</sup> Lucia Guaita,<sup>2</sup> Pascale Hibon,<sup>1</sup> Boris Häußler,<sup>1</sup> Kyoung-Soo Lee<sup>3</sup>, Vandana Ramakrishnan<sup>3</sup>, Ankit Kumar<sup>2</sup>, Nelson Padilla<sup>4</sup>, Nicole M. Firestone<sup>5</sup>, Hyunmi Song<sup>6</sup>, Maria Celeste Artale<sup>2</sup>, Ho Seong Hwang<sup>7,8</sup>, Paulina Troncoso Iribarren<sup>9</sup>, Caryl Gronwall<sup>10,11</sup>, Eric Gawiser<sup>5</sup>, Julie Nantais<sup>2</sup>, Francisco Valdes<sup>12</sup>, Changbom Park<sup>13</sup>, Yujin Yang<sup>14</sup>

<sup>1</sup> European Southern Observatory, Alonso de Córdova 3107, Vitacura, Santiago de Chile, Chile  
e-mail: akriti.ramnee@gmail.com

<sup>2</sup> Universidad Andres Bello, Facultad de Ciencias Exactas, Departamento de Física, Instituto de Astrofísica, Fernandez Concha 700, Las Condes, Santiago RM, Chile

<sup>3</sup> Department of Physics and Astronomy, Purdue University, 525 Northwestern Avenue, West Lafayette, IN 47907, USA

<sup>4</sup> Instituto de Astronomía Teórica y Experimental (IATE), CONICET-UNC, Laprida 854, X500BGR, Córdoba, Argentina

<sup>5</sup> Department of Physics and Astronomy, Rutgers, the State University of New Jersey, Piscataway, NJ 08854, USA

<sup>6</sup> Department of Astronomy and Space Science, Chungnam National University, 99 Daehak-ro, Yuseong-gu, Daejeon, 34134, Republic of Korea

<sup>7</sup> Department of Physics and Astronomy, Seoul National University, 1 Gwanak-ro, Gwanak-gu, Seoul 08826, Republic of Korea

<sup>8</sup> SNU Astronomy Research Center, Seoul National University, 1 Gwanak-ro, Gwanak-gu, Seoul 08826, Republic of Korea

<sup>9</sup> Universidad Central de Chile, Avenida Francisco de Aguirre 0405, 171-0614 La Serena, Coquimbo, Chile

<sup>10</sup> Department of Astronomy and Astrophysics, The Pennsylvania State University, University Park, PA 16802, USA

<sup>11</sup> Institute for Gravitation and the Cosmos, The Pennsylvania State University, University Park, PA 16802, USA

<sup>12</sup> NSF's National Optical-Infrared Astronomy Research Laboratory, 950 N. Cherry Ave., Tucson, AZ 85719, USA

<sup>13</sup> Korea Institute for Advanced Study, 85 Hoegi-ro, Dongdaemun-gu, Seoul 02455, Republic of Korea

<sup>14</sup> Korea Astronomy and Space Science Institute, 776 Daedeokdae-ro, Yuseong-gu, Daejeon 34055, Republic of Korea

Received XX XX, 2024; accepted XX XX, 2024

### ABSTRACT

**Aims.** The aim of this study is to search for quiescent galaxies within the 2-deg<sup>2</sup> COSMOS field at a redshift of approximately 3.1, and to analyze their environment. By investigating the variation in the quenched fraction and the physical properties of the quiescent galaxies with respect to their local environment, protoclusters, and filaments, we seek to understand the relationship between galaxy quenching and environmental factors. This research presents a wide-area statistical analysis of quiescent galaxies, examining their distribution and characteristics within different environmental contexts, to contribute to a broader understanding of galaxy evolution at high redshift.

**Methods.** We use data from the One-hundred-square-degree DECam Imaging in Narrowbands (ODIN) survey and the COSMOS2020 catalog to identify 24 massive quiescent galaxies at redshifts  $\sim 3.1$ . To derive the star formation histories (SFHs) and quenching timescales of these galaxies, we perform spectral energy distribution (SED) fitting using the BAGPIPES code. The galaxy environment is characterized using Voronoi Tessellation-based density maps, utilizing two independent density tracers: Lyman- $\alpha$  Emitters from ODIN and photometrically selected galaxies from the COSMOS2020 catalog.

**Results.** We have identified 24 photometric quiescent galaxies at  $z \approx 3.1$ . These discovered galaxies are massive with stellar mass  $\geq 10^{10.6}$  and we refer to them as massive quiescent galaxies (MQGs). The MQGs we have identified share a common SFH characterized by a massive starburst and a short quenching timescale ( $\leq 400$  Myr). The quenching timescale of MQGs is consistently short, typically less than 500 million years, suggesting a rapid and ubiquitous quenching mechanism. There is no observed correlation between the quenching timescale and the environmental density. Similarly, no correlation between the quenched fraction and the local density is observed. We also find no evidence of correlation of the MQGs with the more large-scale environment such as protoclusters and filaments. The MQGs do not follow a special distribution relative to the filaments and protoclusters discovered in the density maps. Some MQGs are found on gas-rich filaments, but they are not being rejuvenated, indicating a gas-heating mechanism. These results imply that quenching mechanisms are likely driven by similar physical processes independent of their environments. Internal processes, such as AGN feedback, virial shocks or morphological quenching, appear to be more crucial in quenching at high redshifts than environmental factors like galaxy mergers and interactions.

**Key words.** Galaxies: high-redshift – Galaxies: evolution – Galaxies: quenching – Galaxies: massive

## 1. Introduction

Observations and simulations have shown a clear bimodality in various properties of galaxies such as their colors, morpholo-

gies, and star formation rates (SFRs) (Dressler 1980). Quiescent galaxies are characterized by redder colors and typically a spheroidal morphology, whereas star-forming galaxies exhibit bluer colors and typically show disk-like morphology. There is a

gap in our understanding of the mechanisms that cause the star formation in bluer galaxies to stop, quenching them into the redder quiescent galaxies.

Quenching mechanisms are generally categorized as mass quenching or environmental quenching. Mass quenching refers to internal processes that correlate with the stellar mass of a galaxy, such as stellar feedback and AGN (e.g., Croton et al. 2006; Ceverino & Klypin 2009; Fabian 2012; Cicone et al. 2014). Environmental quenching refers to external processes such as ram pressure stripping (e.g., Gunn & Gott III 1972), strangulation (Larson 1990), and galaxy harassment (Moore et al. 1996; Park & Hwang 2009) which depend on the environment in which the galaxy resides. Although both mass and environmental quenching affect the cessation of star formation, their relative importance depends on the mass of the galaxy and the cosmic epoch. In the local universe, there is a well-established relation between SFR and environment density such that quenched galaxies preferentially occur in dense environments such as clusters. In contrast, star-forming galaxies predominantly exist in relatively low-density environments. This is because in local virialized clusters, environmental processes accelerate the quenching of galaxies, thereby increasing the fraction of quenched galaxies. Galaxies have been in clusters for several billion years, which gives enough time for environmental processes to remove or heat cold gas from galaxies (Boselli & Gavazzi 2006).

In recent years, the existence of quiescent galaxies (QGs) at redshifts  $z \sim 3-4$  (e.g., Spitler et al. 2014; Straatman et al. 2014; Girelli et al. 2019; Carnall et al. 2018, 2023) has been corroborated by spectroscopic confirmations (e.g., Glazebrook et al. 2017, 2022; Schreiber et al. 2018; D'Eugenio et al. 2020; Nanayakkara et al. 2024). At low redshift ( $z < 1$ ), quenching processes typically occur on timescales of several billion years (Mao et al. 2022). However, at redshift = 3, the universe is only about 2 billion years old, meaning that quiescent galaxies at redshift  $> 3$  have not had large timescales available to undergo quenching, which are required for processes that typically quench galaxies at low redshifts. This raises the question of what processes quenched galaxies at  $z > 3$ . The role of the environment in quenching in the early universe remains unclear. Some studies suggest that high-density environments promote star formation and are dominated by starburst (Casey 2016; Calvi et al. 2023), whereas other protoclusters have been found to be dominated by quiescent galaxies (Ito et al. 2023; Tanaka et al. 2024). In this study, we conducted a statistical analysis of quiescent galaxies and their environments in the COSMOS field at redshift 3.1 to determine if there is a systematic relationship between the environment and quenching.

To trace the environmental density, we have used two tracers, the photo- $z$  selected galaxies in the COSMOS2020 catalog (Weaver et al. 2021), and Lyman- $\alpha$  emitting galaxies (LAEs). The Ly $\alpha$  emission line ( $\lambda_{rest-frame} \approx 1216\text{\AA}$ ) is the strongest recombination line of neutral Hydrogen and it has been used to trace star formation, AGN activity, and the gravitational collapse of dark matter halos at redshift  $\geq 2$  (Ouchi et al. 2020). Given the wavelength of Ly $\alpha$  emission, LAEs can be detected up to  $z \sim 6$  using ground-based photometric surveys, making them an ideal tool for tracing the underlying density distribution and the large-scale structure over wide areas (e.g., Hu & McMahon 1996; Ouchi et al. 2003; Gawiser et al. 2007; Kovač et al. 2007). With the photo- $z$  selected galaxies and LAEs we create two density maps that we use to study the environment of MQGs.

Some studies based on simulations have suggested that AGN feedback is the primary quenching mechanism for high-redshift

MQGs (Kurinchi-Vendhan et al. 2023; Hartley et al. 2023). Kurinchi-Vendhan et al. (2023) found in the IllustrisTNG simulation that the number of merger events in a galaxy's history is not sufficient to distinguish between quiescent and star-forming galaxies, and that AGN feedback is required to quench the galaxy. However, Kimmig et al. (2023) recently showed, using the Magneticum simulation, that while AGN-driven gas removal quenches galaxies, quenching is also influenced by the environment. They found that for a galaxy to be quenched, it must reside in a significant underdensity, which prevents gas replenishment. The aim of this study is to observationally assess the extent of the environmental impact on galaxy quenching at redshift 3.1.

To look for the quiescent galaxies we have used archival photometric data in the optical, near- and mid-IR bands. The data used to select the galaxies and make density maps criteria are given in Sections 2.1 and 2.2. The SED fitting analysis needed to determine the passive nature of MQGs is described in Section 2.4. We describe the selection of quiescent galaxies in Section 2.5. In section 3.2 we describe the density maps constructed using LAEs and photo- $z$  selected galaxies. A summary of the results is presented in Section 3. A discussion of our results and a comparison with previous observations and current simulations is presented in Section 4. Throughout this paper, a standard cold dark matter cosmology is adopted with the Hubble constant  $H_0 = 70 \text{ km s}^{-1} \text{ Mpc}^{-1}$ , the total matter density  $\Omega_M = 0.3$  and the dark energy density  $\Omega_\Lambda = 0.7$ . All magnitudes are expressed in the AB system and log is the base 10 logarithm, if not otherwise specified.

## 2. Data & Methods

In this section, we describe the archival and new observed data that we have used to select galaxies at  $z \sim 3.1$ . These galaxies are used to make density maps to trace the large-scale environment as described in Sections 2.6, 2.7 and 2.8. We also describe here the SED fitting method used to select MQGs from the selected galaxies.

### 2.1. The One-hundred-deg<sup>2</sup> DECam Imaging in Narrowbands Survey

The One-hundred-square-degree DECam Imaging in Narrowbands (ODIN) survey uses Lyman-alpha (Ly $\alpha$ ) emitting galaxies to trace the cosmic structures and overdensities at the following redshift slices:  $z \sim 4.5, 3.1, 2.4$  ( $t_{age} = 1.3, 2.0, 2.7$  Gyr since the Big Bang, respectively). ODIN uses narrow-band and broadband photometry to find LAEs at these redshifts. The adopted *N419*, *N501*, and *N673* filters have central wavelengths of 419 nm, 501 nm and 673 nm, respectively, with full width at half maxima (FWHM) of 7.5 nm, 7.6 nm and 10.0 nm, respectively, which cover the Lyman-alpha line at the redshifts mentioned above. LAEs are selected as narrow-band excess compared to the existing broad-band data from Hyper-Support-Cam Subaru. ODIN aims to select more than 100,000 LAEs at the three cosmic epochs (Lee et al. 2024).

The survey design and LAE selection in the ODIN survey are described in detail in Lee et al. (2024) and Firestone et al. (2023), respectively. In this paper, we use the LAEs selected in the Cosmic Evolution Survey (COSMOS) field (Scoville et al. 2007) as described in Firestone et al. (2023). We concentrate on redshift  $\sim 3.1$  in the COSMOS field because the ODIN observations at this redshift (*N501* filter) have been fully acquired and reduced and

the LAE density map has been published (Ramakrishnan et al. 2023).

## 2.2. Publicly available data

The COSMOS field is a 2-square-degree field with the deepest available near-infrared wide-field coverage (Scoville et al. 2007; McCracken et al. 2012; Weaver et al. 2021; Dunlop et al. 2023). The COSMOS2020 photometric catalog (Weaver et al. 2021), includes ultra-deep optical data from Hyper-Suprime-Cam (Aihara et al. 2019), ultra-deep near-infrared UltraVISTA data (Dunlop et al. 2023), and *Spitzer*IRAC data (Weaver et al. 2021). The deep Ultra-VISTA data and *Spitzer* data are well suited to look for optically faint galaxies like MQGs. We use the COSMOS2020 catalog, which is produced using a profile fitting photometry method (known as the COSMOS “FARMER” catalog). The details of the photometry and SED fitting for this catalog are described in Weaver et al. (2021). We also use photometric redshifts estimated from LePhare (Arnouts et al. 1999), provided in the catalog.

## 2.3. Selection of galaxies at redshift $z \sim 3.1$

For the COSMOS2020 catalog, Weaver et al. (2021) discuss the accuracy of photometric redshifts obtained using the LePHARE code (Arnouts et al. 1999) by comparing them to spectroscopic redshifts. They report that the LePHARE photometric redshifts show a high degree of consistency with the spectroscopic redshifts in the COSMOS field, achieving subpercent photometric redshift accuracy. The precision of photometric redshifts (photo- $z$ ) is approximately  $0.01 \times (1+z)$  for galaxies with  $i$ -band magnitude  $< 22.5$ . For fainter magnitudes, the precision decreases but remains better than  $0.025 \times (1+z)$  for  $i < 25$ . Given this good quality of photo- $z$  in the COSMOS2020 catalog, we used the LePHARE photo- $z$  to select the sample of galaxies at  $z \sim 3.1$ .

Our redshift selection criterion requires that the photometric redshift at the minimum chi-square is  $3.004 \leq z_{phot} \leq 3.224$ , and 68 percent of the redshift probability distribution function lying within the redshift range,  $3.004 < z < 3.224$ . With this criterion, we select 6431 galaxies. This selection ensures a clean sample with low uncertainty in the redshift range. To select the quiescent galaxies from this sample, we perform the SED fitting using the photometric data available in the COSMOS2020 catalog.

## 2.4. SED fitting using BAGPIPES

The Bayesian Analysis of Galaxies for Physical Inference and Parameter Estimation (BAGPIPES, Carnall et al. 2018, 2023) is a state-of-the-art Python code to model galaxy spectra and fit spectroscopic and photometric observations simultaneously. In recent years, BAGPIPES has been used successfully in the literature to study MQGs (see, e.g., Jin et al. 2024). We use the BAGPIPES code to fit the COSMOS2020 SED of all 6431  $z \approx 3.1$  galaxies and estimate their specific star formation rate (sSFR).

For our study, we perform spectral energy distribution (SED) fitting utilizing all 29 photometric bands available from the COSMOS2020 catalog. We adopt a double power-law star formation history (SFH) model, which effectively captures the rising and declining phases of the SFH with two distinct power-law slopes. The functional form of the SFH is given by:

$$\text{SFR}(t) \propto \left[ \left( \frac{t}{\tau} \right)^\alpha + \left( \frac{t}{\tau} \right)^{-\beta} \right]^{-1} \quad (1)$$

where  $\alpha$  and  $\beta$  are the falling and rising slopes respectively, and  $\tau$  is related to the time at which star formation peaks. Carnall et al. (2018) conducted a comparative study of various star-formation history (SFH) parameterizations for quenched galaxies generated using the MUFASA simulation (Davé et al. 2016). They found that for quenched galaxies, the classical exponentially declining SFH model tends to overestimate stellar masses by an average of 0.06 dex ( $\approx 15\%$ ), with around 80% of the objects having overestimated stellar masses. Additionally, this model underestimates the formation and quenching of redshifts by approximately 0.4 Gyr on average. In contrast, the double power-law model showed significantly better agreement with observed data, yielding more accurate estimates for stellar mass, formation redshift, and quenching timescale. Specifically, the stellar-mass estimates were offset by only 0.02 dex, and the bias in the median quenching timescale was reduced to 100 Myr. The better agreement achieved with using the double power law model led us to take this model forward for use in fitting our COSMOS2020 sample.

We follow the method described in Carnall et al. (2023) for the SED fitting of our galaxies using BAGPIPES. We assume the 2016 updated version of the Bruzual & Charlot (2003) stellar population models (Chevallard & Charlot 2016) using the MILES stellar spectral library (Sanchez-Blazquez et al. 2006; Falcón-Barroso et al. 2011) and the updated stellar evolutionary tracks of Bressan et al. (2012) and Marigo et al. (2017). Nebular line and continuum emissions are implemented using an approach based on the CLOUDY photoionization code. We fix the ionization parameter to  $U = 10^{-3}$ . Dust attenuation is taken into account using the model proposed by Salim & Narayanan (2020). This model has a variable slope that is parameterized with a power-law deviation,  $\delta$ , from the Calzetti et al. (2000) model. Given the good agreement between the LePhare photometric and spectroscopic redshifts, we fixed the redshift prior in the fit to lie between the lower and upper limits that encompass 68% of the redshift distribution around the central value. Table 1 shows the priors and range for all the free parameters of the SED fitting.

An example of the SED fitting and its corresponding results is shown in Figure 1. The output of BAGPIPES is the star formation history and a list of physical parameters of the galaxy, such as age of the stellar population, current star formation rate, star formation history, timescale of quenching, dust, metallicity, and stellar mass. The SEDs of all the selected MQGs are shown in the Appendix A.

## 2.5. Selection of quiescent galaxies

To separate star-forming and quiescent galaxies, we use a redshift-dependent cut in the specific star formation rate as has been widely applied in the literature (e.g., Pacifci et al. 2016; Carnall et al. 2023). We define quiescent galaxies as those that have

$$\log(\text{sSFR} + \sigma_{\text{sSFR}}) \leq \frac{0.2 \text{ yr}}{t_{\text{age}}} \quad (2)$$

$$\text{where } \frac{0.2}{t_{\text{age}}} = -10.01$$

where  $\sigma_{\text{sSFR}}$  is the uncertainty in the specific star formation rate, and  $t_{\text{age}}$  is the age of the Universe at  $z = 3.1$ . This threshold corresponds to the UVJ color selection criteria for quiescent galaxies at  $z < 0.5$  as introduced by Williams et al. (2009). In order to

Table 1: The priors of the free parameters of the BAGPIPES model we use to fit photometric data.

Component	Parameter	Range	Prior
General	Total stellar mass formed ( $M_*/M_\odot$ )	(1, $10^{13}$ )	Logarithmic
General	Stellar and gas-phase metallicity ( $Z/Z_\odot$ )	(0.2, 2.5)	Logarithmic
Star-formation history	Double-power-law falling slope ( $\alpha$ )	(0.01, 1000)	Logarithmic
Star-formation history	Double-power-law rising slope ( $\beta$ )	(0.01, 1000)	Logarithmic
Star-formation history	Double power-law turnover time ( $\tau/\text{Gyr}$ )	(0.1, $t_{\text{obs}}$ )	Uniform
Dust attenuation	V-band attenuation ( $A_V/\text{mag}$ )	(0, 8)	Uniform
Dust attenuation	Deviation from Calzetti et al. (2000) slope ( $\delta$ )	(-0.3, 0.3)	Gaussian
Dust attenuation	Strength of 2175 Å bump ( $B$ )	(0, 5)	Uniform

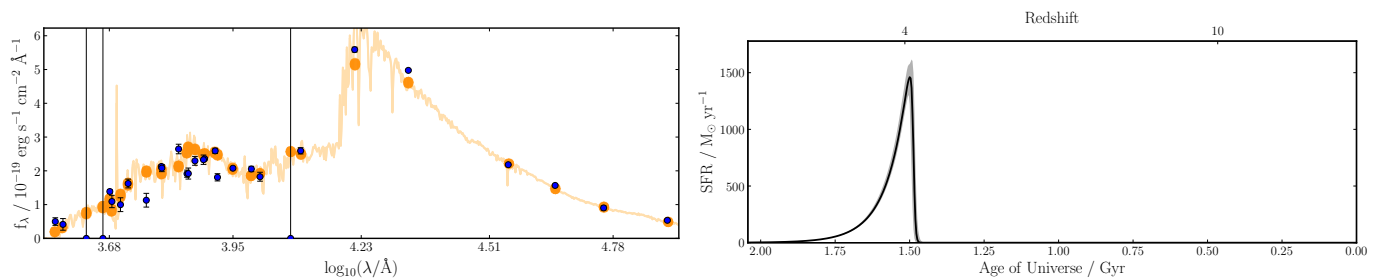


Fig. 1: Left: SED fitting of a massive quiescent galaxy obtained with the BAGPIPES code and using the double power law star formation history model. The blue points with error bars represent the input photometry from the COSMOS2020 catalog. The 16th to 84th percentile range for the posterior spectrum and photometry are shaded orange line. The orange points correspond to the models convolved with the photometric band filters. Right: Star-formation history of the massive quiescent galaxy shown in right panel. The black line indicates the median of the posterior probability distribution of the star formation history and the gray shaded area shows the 68% confidence range for the same.

remove eventual contaminants, we visually inspect all 43 SED fits selected using Equation 2.

We exclude objects that are visible in short-wavelength imaging, below the position of the Lyman break at  $z \approx 3.1$ . The SED of a MQG at  $z = 3.1$  is expected to be faint in the optical bands and bright in the JHK bands, showing a significant Balmer break at  $1.49 \mu\text{m}$ . SED bright in the optical bands could imply that either the fitted redshift is incorrect or the star formation rate of the galaxy is not constrained well. Examples of rejected SEDs are shown in the Appendix A. We also cross-match our MQG candidates with the publicly available spectroscopic data. From the VIMOS Ultra Deep Survey (Lemaux et al. 2014; Le Fèvre et al. 2013) database, we were able to conclusively confirm the redshift of one of our MQGs. The confirmed galaxy is at  $z=3.0661$  and shows a clear CIV emission line (Lemaux et al. 2014) in the spectrum that may be due to an AGN. Our final sample is composed of 24 bonafide QGs. In Appendix A we show the SEDs of the entire selected MQG sample.

## 2.6. Voronoi Monte Carlo Map construction from the COSMOS2020 catalog

We adopted the Voronoi Monte Carlo (VMC) mapping technique to measure galaxy density across the entire COSMOS field within our redshift range. This approach has been thoroughly examined and validated in previous studies in the literature (eg. Shah et al. 2024; Hung et al. 2020; Lemaux et al. 2018; Cucchiati et al. 2018; Forrest et al. 2020), demonstrating its robustness and reliability. The major advantage of the VMC mapping is its ability to cover a wide dynamical range in densities, i.e. allowing the detection of both very high and very low densities, without assuming any prior on the shape of the density field. Hence, it is a non-parametric and scale-independent method.

In the simple Voronoi tessellation method, a 2D plane is divided into a number of cells such that each cell is associated with an object. Each cell is defined as the collection of all the points closer to that object than to any other object. Therefore, more crowded regions will have smaller cells than less crowded regions. The density associated with each cell is calculated using the area of each cell as explained below. To take into account the variation of redshift within our redshift range, instead, we used the VMC technique described in Hung et al. (2020) representing an improvement over the standard Voronoi technique. The resultant VMC map is shown in the left panel of Figure 2. The main steps are:

- We constructed a series of overlapping redshift slices within our entire redshift range of  $3.004 \leq z \leq 3.224$ . The width of each redshift slice ( $z$ -slice) is equal to the median uncertainty on the photometric redshift of our QG sample, i.e. 0.04.
- We assigned a photometric redshift probability weight to each galaxy in each slice. The percentage of the redshift probability distribution function ( $z$ -pdf) lying in the  $z$ -slice is the weight of a galaxy for a given slice. For this, we assumed that all galaxies have a Gaussian  $z$ -pdf.
- We generate a random number for each galaxy. The random number lies between the minimum weight and the maximum weight of all the galaxies for a slice. If the weight of a galaxy is greater than the random number, then it is accepted. Thus, we have a set of accepted galaxies for each  $z$ -slice.
- For each  $z$ -slice, we then generate a simple Voronoi map. The average of all 12  $z$ -slice Voronoi maps is the final Voronoi map we use in this study.

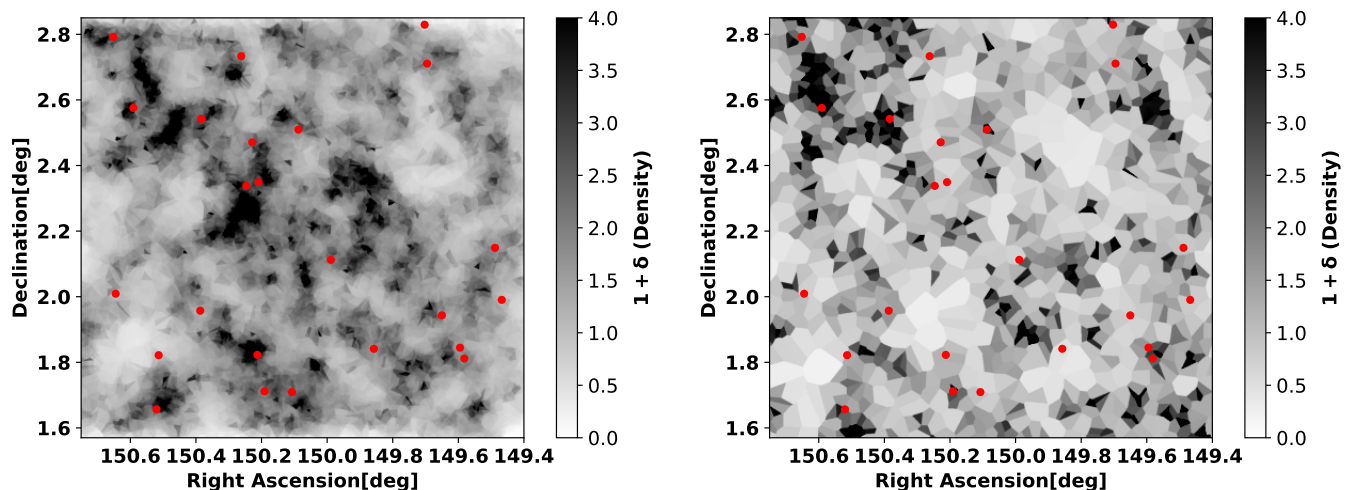


Fig. 2: Density map traced by the galaxies selected from COSMOS2020 (Left) and the LAE (Right) catalogs, by using the Voronoi Monte Carlo Technique (Section 2.3). The color bar represents the normalized density calculated in Section 2.8. The red dots represent the MQGs.

### 2.7. Voronoi Map construction from the ODIN-LAE catalog

In order to create the LAE Voronoi map, we assume that the redshifts of all our LAEs are fixed at  $z = 3.1$ . This is because the narrow-band technique used to find the LAEs is very secure, with a redshift range of 0.062 (Firestone et al. 2023). Of the ODIN LAEs that have confident redshift measurements from DESI,  $\sim 97\%$  had the correct redshift classification for being in the N501 filter. The LAE map and the structures discovered therein were published in Ramakrishnan et al. (2023). The right panel of Figure 2 shows the LAE Voronoi map.

### 2.8. Density Estimation from the Voronoi Maps

Following the methodology described in the literature (e.g., Cucciati et al. 2018; Lemaux et al. 2018; Hung et al. 2020), we create a pixelated surface density map. This is done by populating the field with a uniform grid of points, where the grid spacing is set to  $\approx 70$  ckpc, which is much smaller than Voronoi cells. Each pixel within a Voronoi cell is assigned a surface density. The surface density in a Voronoi cell  $(i, j)$ ,  $\Sigma_{(i,j)}$ , is calculated using the area of a Voronoi cell ( $A_v$ ) as follows:

$$\Sigma_{(i,j)} = \frac{1}{A_v} \quad (3)$$

The normalized local density,  $(1+\delta)$ , in a Voronoi cell  $(i, j)$  is then estimated as:

$$\log(1 + \delta) = \log\left(1 + \frac{\Sigma_{(i,j)} - \tilde{\Sigma}}{\tilde{\Sigma}}\right) \quad (4)$$

where  $\Sigma_{(i,j)}$  is the given Voronoi cell's density and  $\tilde{\Sigma}$  is the median density of all the Voronoi cells in the redshift slice (Figure 2). As discussed in various studies, these local density estimates correlate well with other density metrics and accurately trace known overdensity structures. We repeat this process for the LAE Voronoi map to construct an LAE density map. As described in (Ramakrishnan et al. 2023), the size of a pixel is 120 ckpc on a side for the LAE density map.

## 3. Results

### 3.1. Number density and physical properties of quiescent galaxies

We identify 24 MQG candidates at  $z \approx 3.1$ . One of them has been previously identified by Ito et al. (2023). The remaining 23 are promising new photometric candidates. The total volume surveyed, excluding star masks, covered by the COSMOS2020 catalog, is  $8.71 \times 10^5$  cMpc<sup>3</sup>. Therefore, we calculate the number density of MQGs as  $2.87 \times 10^{-5}$  galaxies cMpc<sup>-3</sup>, consistent with the observed number densities reported in the literature (Straatman et al. 2014; Schreiber et al. 2018; Merlin et al. 2019; Carnall et al. 2023), as well as estimated from simulations, such as IllustrisTNG300 (Valentino et al. 2020).

The BAGPIPES code gives the star formation histories (SFH) that best reproduce the observed photometry of a galaxy as an output. Examples of our MQGs are shown in Figure 1, where we can see that the SFHs have a starburst-like shape within the first 500 Myr followed by a rapid decline. The BAGPIPES code estimates the time of formation ( $t_{form}$ ) and the time of quenching ( $t_{quench}$ ) for a galaxy. We define the quenching timescale as follows:

$$T_q = t_{quench} - t_{form} \quad (5)$$

The similar quenching timescale of the majority of our galaxies could suggest they have been affected by a common quenching mechanism.

There is an MQG that is characterized by a longer quenching timescale of  $\approx 0.9$  Gyr. Unlike the rest, it could be possible that this galaxy did not undergo a strong starburst in its star formation history and has an SFR peak of only  $\sim 150 M_{\odot} \text{yr}^{-1}$ . This particular galaxy is an outlier and may have a different kind of quenching mechanism. This galaxy lies in an underdense region, and environmental processes like galaxy-galaxy interactions and mergers may be less likely to quench this galaxy.

### 3.2. Density Maps at $z = 3.1$

The photo- $z$  and LAE Voronoi maps are shown in Figure 2. With the density maps, we find overdense structures that may eventu-



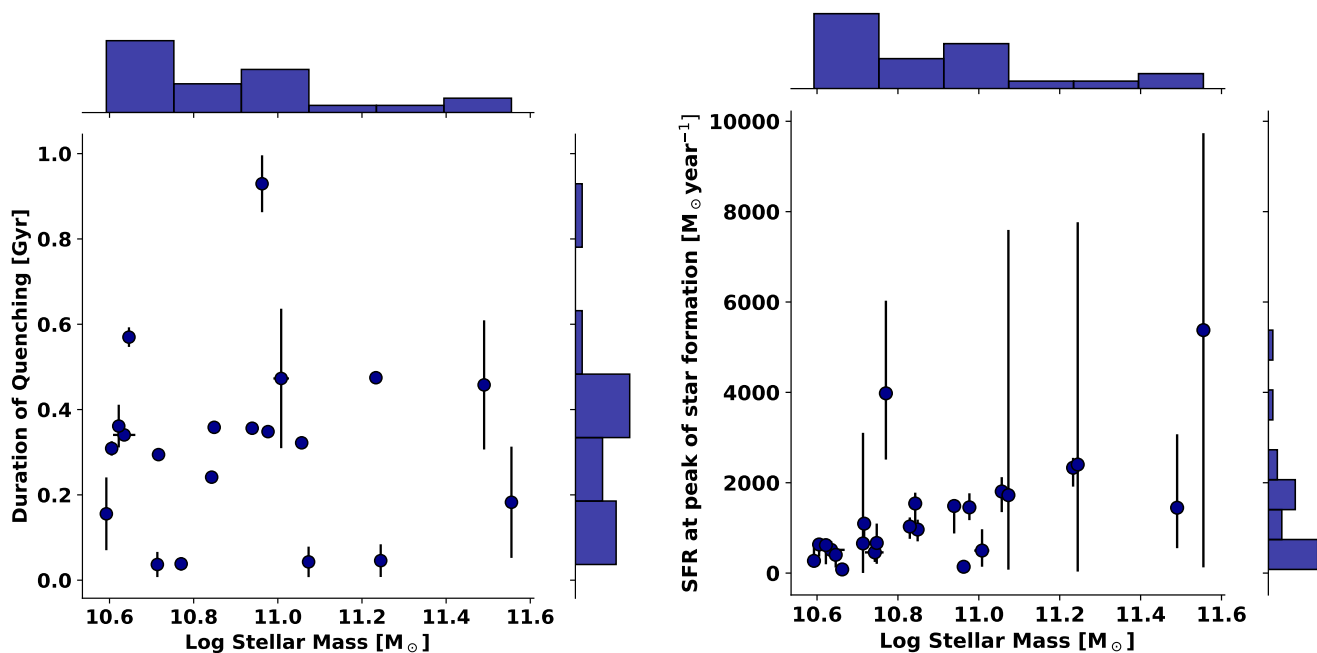


Fig. 3: Left: The time it takes to quench the MQGs (as defined in Equation 3.1) versus the stellar mass estimated using BAGPIPES. The median duration of quenching is  $\sim 350$  Myr and is consistent for all MQGs. The log stellar mass ( $M_{\odot}$ ) is always  $\geq 10.6$ . Right: The star formation rate at the peak of star formation in the history of the MQG vs the stellar mass. The peak SFR increases linearly with mass indicating a stronger starburst for more massive galaxies.

ally evolve into present-day galaxy clusters. For structure detection, we use SEP (Barbary 2016), a Python implementation of SExtractor (Bertin & Arnouts 1996) software. The number of detected structures depends strongly on the detection threshold (DETECT\_THRESH) and minimum area (DETECT\_MINAREA). Ramakrishnan et al. (2023) find that a DETECT\_THRESH of  $4.5\sigma$  and DETECT\_MINAREA of 3000 pixels ( $\approx 40$  cMpc $^2$ ) yield a contamination rate of 20%. We follow this prescription of Ramakrishnan et al. (2023) to find the overdense structures from the surface density maps. In Figure 4, we show the structures detected in the LAE and COSMOS2020 Voronoi maps, respectively.

There are some important differences between the LAE and the COSMOS2020 map. To discuss them in detail, we name some of the overdensities in capital letters. The large overdensities at  $\delta \approx 2.3^{\circ}$  (B and C in Figure 4) detected in the COSMOS2020 map are not detected in the LAE map. The large overdensity at  $\alpha = 149.6^{\circ}$  detected in the LAE map (D) is not detected in the COSMOS2020 map. The group of overdensities at  $\alpha \approx 150.6^{\circ}$  (A) is detected in both maps. The reason for the difference in the appearance of the overdensities may be due to the redshift ranges. The photo- $z$  galaxies are selected to be in the range  $3.004 \leq z \leq 3.224$ , while the LAEs lie in a narrower range of  $\Delta z = 0.062$ , centered at  $z = 3.124$  (Lee et al. 2024). Therefore, the new structures in the photo- $z$  map could be just outside the very narrow range of the LAE map. The structures detected in the density maps are promising photometric protocluster candidates. Follow-up spectroscopy of the constituent galaxies of these protoclusters could confirm their exact redshift and 3-D shape.

Only 6 of 24 MQGs are located within protocluster candidates discovered in either the LAE or photo- $z$  maps, which represents just 25% of the MQG candidates. This suggests that

processes that typically occur in dense environments, such as ram-pressure stripping (Boselli et al. 2022), thermal evaporation (Cowie & Songaila 1977), and galaxy mergers (Rodríguez Montero et al. 2019), may not always be necessary for galaxy quenching.

We compared the distribution of MQGs with that of the entire galaxy sample in relation to the protocluster candidates. Figure 5 displays the two distributions. To determine whether the MQGs and all galaxies follow the same distribution, we performed the Anderson-Darling test. The test was unable to reject the null hypothesis that the two distributions are the same distribution. This further indicates that MQGs follow the same distribution with respect to protoclusters as any other type of galaxy. We interpret this as evidence that environmental processes, which are more common in protoclusters, are not the dominant quenching mechanism. This contrasts with the local universe, where quiescent galaxies are predominantly found in the centers of clusters because environmental quenching processes are the primary quenching mechanism in the local universe.

Figures 6 and 7 show the quenching time scale and the  $SFR_{peak}$  vs. the environmental density in the photo- $z$  map and the LAE map, respectively. We show that neither the quenching timescale nor the SFR at the peak of star formation activity depends on the local environment density. In other words, the SFH is independent of the environmental density. This suggests that the mechanisms responsible for star formation in MQGs do not depend on the environment.

### 3.3. Quiescent fraction and the environment

The quiescent fraction is described as the proportion of MQGs to the complete count of galaxies present within a specified den-

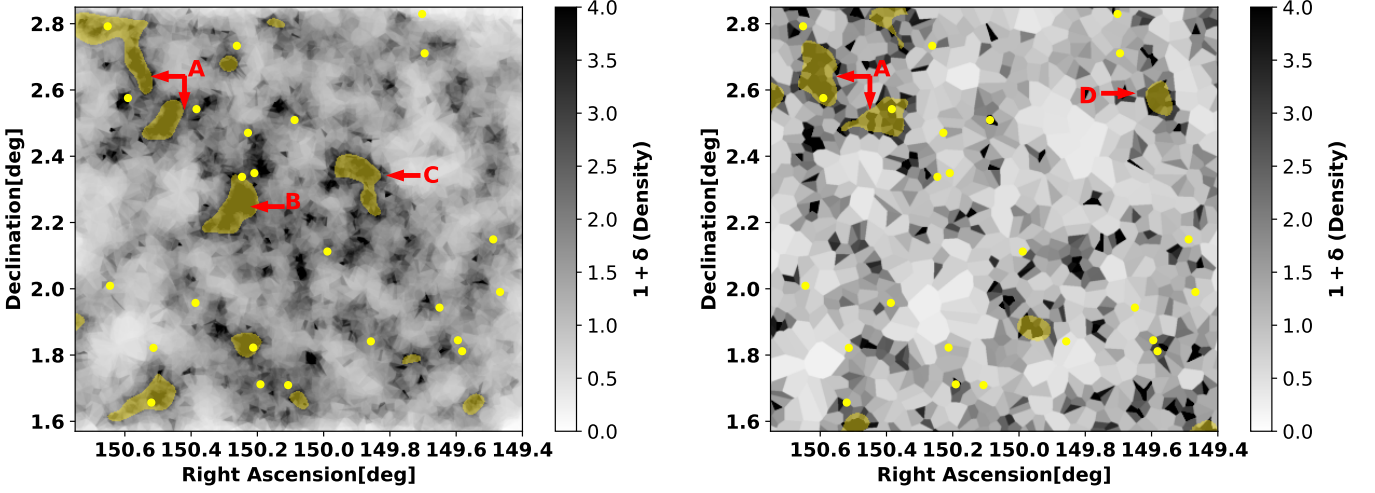


Fig. 4: Yellow shaded regions represent structures identified by running Source Extractor in the COSMOS2020 (left) and in the LAE (right) maps. Yellow dots represent MQGs. The color bar scales the  $\log(1+\delta)$  density for both maps as in Figure 2. The A, B, C, and D letters indicate some major overdensity groups discovered in either one or both maps.

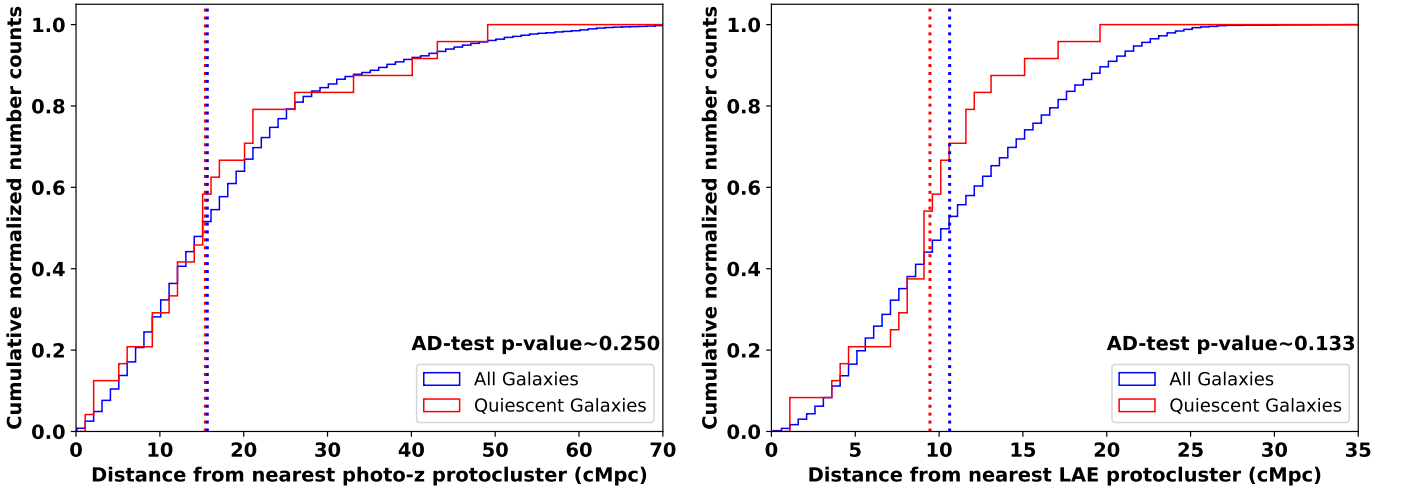


Fig. 5: Left: The distribution of the distances of MQGs, and photo-z selected galaxies to the photo-z protocluster centers. Right: The distribution of the distances of MQGs, and photo-z selected galaxies to the LAEs protocluster centers. The dotted lines show the median distribution for each type of galaxy. The p-value of the Anderson-Darling test comparing MQGs with the all galaxy distribution is also displayed.

sity bin. Figure 8 shows the quiescent fraction as a function of local density. By local density, we refer to the density within the pixel of the Voronoi map at which the MQG resides. The resolution of the photo-z density map and the LAE density map is  $70 \text{ ckpc pixel}^{-1}$  and  $120 \text{ ckpc pixel}^{-1}$  respectively. The uncertainty in the quiescent fraction is obtained using the method described by Gehrels (1986), which provides convenient tables and approximate formulas to calculate confidence limits based on Poisson and binomial statistics. This method is widely used in astronomy for estimating uncertainties with small-number statistics. We used equations 9 and 12 from Gehrels (1986) to calculate these uncertainties, which provide the upper ( $\lambda_u$ ) and lower limit ( $\lambda_l$ ) to a measured quantity according to Poisson statistics

as follows:

$$\lambda_u = n + S \sqrt{n+1} + \frac{S^2 + 2}{3} \quad (6)$$

$$\lambda_l = n \left( 1 - \frac{1}{9n} - \frac{S}{3\sqrt{n}} \right)^3 \quad (7)$$

Here  $n$  is the number of observed events (or counts). It is the observed value for which the confidence limits are calculated.  $S$  is a Poisson parameter whose value is listed in Gehrels (1986) for different confidence levels.

To quantify the observed correlation between the quenched fraction and the local density in both the COSMOS2020 map and the LAE map, we employ the Spearman correlation coefficient.

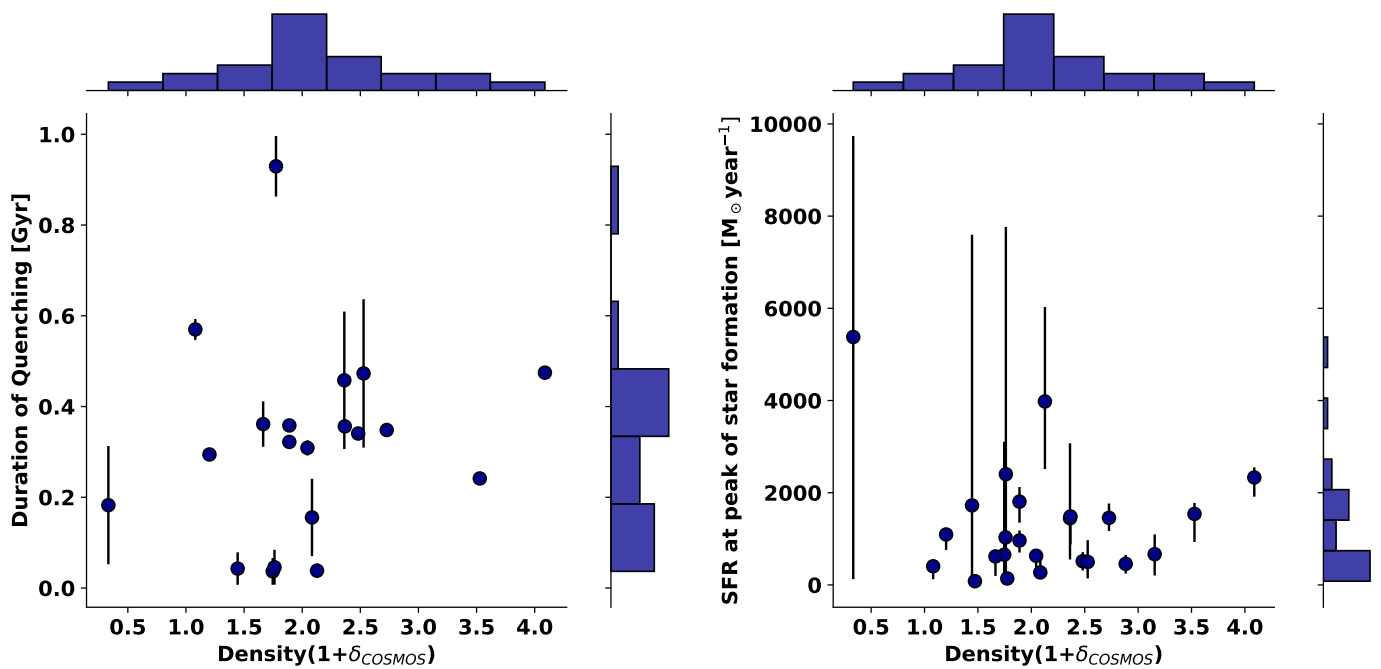


Fig. 6: Left: Quenching timescale vs density from the COSMOS2020 VMC map. Right: SFR at peak of star formation vs density.

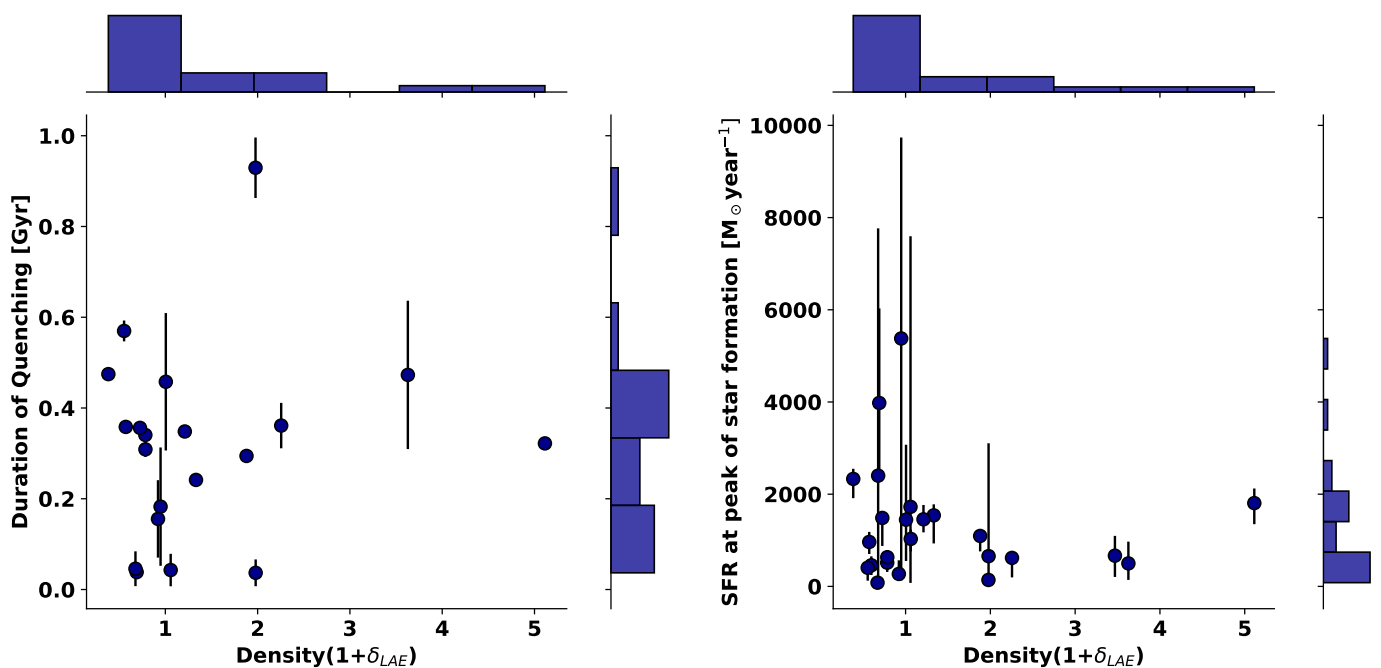


Fig. 7: Left: Quenching timescale vs density from the LAE density map. Right: SFR at the peak of star formation vs density.

Taking into account the uncertainty in the quiescent fraction, we calculate a weighted Spearman coefficient. This involves sampling the quenched fraction within the bounds of the uncertainty 3000 times. For each sample, we compute the Spearman correlation coefficient. Finally, we determine the mean and standard deviation of the computed coefficients, providing a robust measure of the correlation while accounting for the associated uncertainties. We obtain a mean Spearman correlation coefficient of  $\approx 0.55$  and a standard deviation of  $\approx 0.4$ . A Spearman coefficient of 0.55 signifies a weak or no correlation. To robustly confirm

a correlation, the coefficient should exceed 0.7, while a value below 0.4 generally suggests the absence of correlation. In our Monte Carlo simulations, we found that 43% of the runs resulted in a correlation coefficient below 0.4, leading us to conclude that there is no dependence on the local density. To validate these statistical results, we performed simulations, generating samples with varying levels of correlation, strong and weak. Our findings indicate that a weak correlation can still be observed even with a small sample size of 25 when using weighted Spearman coef-



Table 2: Number of neighbours of MQG, and all galaxies

Radius [cMpc]	QG	ALL
0.3	$1.18 \pm 0.33$	$1.12 \pm 0.44$
0.5	$1.50 \pm 0.70$	$1.42 \pm 0.71$
1.0	$2.58 \pm 1.50$	$2.45 \pm 1.45$
3.0	$13.90 \pm 4.19$	$11.90 \pm 5.90$
6.0	$36.50 \pm 11.6$	$29.6 \pm 13.35$

**Notes.** The table shows the median  $\pm$  standard deviation of the number of neighbors for circles of different radii in Mpc for MQG, all galaxies.

ficients. Further details, including a more thorough examination of the correlation, can be found in the Appendix A.

The independence of the quiescent fraction of the local density is in agreement with the analysis in Section 3.2, and further suggests that quenching mechanisms in MQGs may not be driven only by environmental processes.

### 3.4. Neighbor count

In the local universe, environmental processes such as mergers and interactions within galaxy groups and clusters typically quench galaxies in high-density environments (Boselli & Gavazzi 2006). To investigate the environment of MQGs at different scales, we counted the number of nearest neighbors within 2-D projected distances ranging from 0.1 to 6 cMpc for all photo-z selected galaxies and all MQGs. Table 2 presents the median values. Figure A.1 in the Appendix A shows the distribution of the number of neighbors for MQGs and for all galaxies in the COSMOS2020 catalog.

From the median values, we conclude that MQGs and all galaxies have similar median values for their number of neighbors. This indicates that MQGs do not have a higher probability of residing in groups or overdense environments at various scales than star-forming galaxies. Secular quenching mechanisms, such as AGN feedback and stellar feedback, which do not necessarily depend on the environment, may play a dominant role in the quenching of galaxies at this epoch at  $z = 3.1$ .

### 3.5. Filaments

Filaments traced by LAEs are recognized as substantial reservoirs of cold gas that can sustain star formation in galaxies. Consequently, it is anticipated that star-forming galaxies will be located on or close to these filaments. Conversely, a negative correlation is expected between MQGs and filaments, as galaxies situated near filaments benefit from a continuous supply of cold gas conducive to star formation. Ramakrishnan et al. (2023) identified these filaments within the COSMOS field using LAEs and the Discrete Persistent Structure Extractor (DisPerSE) code (Sousbie 2011).

It is crucial to note that the redshift range of the LAEs utilized to trace these filaments is very narrow, specifically  $\Delta z = 0.062$ . We do not have the precise spectroscopic redshift for MQGs and photo-z selected galaxies from COSMOS2020 catalog. The redshift range for our MQGs and photo-z selected galaxies is wider and spans  $3.1 \pm 0.12$ . As a result, we can only compute the two-dimensional projected distances of our photo-z sample galaxies relative to the filaments. These distances are measured in arcseconds, where at  $z=3.1$ ,  $1''$  corresponds to 31.27 ckpc. We compare the distributions of MQGs and the entire photo-z selected sample at  $z=3.1$  using the Anderson-

Darling test. Figure 9 displays the filaments detected in the COSMOS field with LAEs, illustrating the spatial distribution of the massive quiescent galaxies relative to these filaments.

The Anderson-Darling test reveals no significant difference between the distributions of MQGs and the full photo-z sample. The median distances of MQGs and photo-z galaxies from the filaments are 9 and 11 cMpc, respectively. This similarity suggests that the probability of a galaxy to be quenched does not depend on its proximity to a filament. We also find some MQGs lying in proximity to gas-rich LAE filaments. Specifically, 9 out of 24 MQGs are located within 5 cMpc of a filament. For these MQGs, the proximity to a gas-rich filament could imply that gas-heating processes, such as virial shock heating or AGN feedback, might be inhibiting star formation rather than cosmic starvation, as filaments are typically rich in gas.

## 4. Discussion

In this work, we have searched for massive quiescent galaxies at  $z \sim 3.1$ , corresponding to an age of the Universe of  $\sim 2$  billion years, studied their physical properties and investigated their relationship with the environment. We discovered 24 MQGs, characterized by  $\log \text{sSFR} < -10.01$  in a  $2 \text{ deg}^2$  area of the COSMOS field. The probed volume corresponds to  $8.71 \times 10^5 \text{ cMpc}^3$ . The number density of MQGs of  $2.87 \times 10^{-5} \text{ galaxies/cMpc}^3$  is consistent with observations and simulations in the literature (Valentino et al. 2020).

We have characterized the environment in the COSMOS field, considering two independent tracers, LAEs and the general galaxy population of the COSMOS2020 catalog, using the Voronoi Tessellation. While there are overdense structures that are common in both these maps, there are large overdense structures which are discovered only in either of the two maps. The reason for this difference could be the redshift precision being different between the 2 samples. We selected galaxies from the COSMOS2020 catalog on the basis of photometric redshifts. The range of this photo-z is  $\approx 3$  to  $3.2$ . This may lead to an overdensity detection which is not co-spatial with LAE-traced structures whose redshift range is very narrow ( $\Delta z=0.06$ ,  $z \approx 3.1$ ).

Our study identifies two protoclusters, which we call B and C, that are present in the photo-z map but absent in the LAE map. Forrest et al. (2023) have discovered protoclusters at positions similar to B and C in their analysis at a slightly higher redshift ( $z \sim 3.32$ ), named S3 and S1 in their analysis. We propose that these two protoclusters detected in our photo-z map could also be the front-end extension of the S1 and S3 protoclusters. Our LAE observations missed these because their narrow redshift range stretches only to 3.11, in contrast to our photo-z range which extends up to 3.2.

LAEs are detected using the narrow-band excess created by the Lyman- $\alpha$  emission line. The absorption of the resonant Lyman-alpha line in a dusty and highly overdense region could make it harder to detect LAEs. The Lyman-alpha IGM transmission is a complex function, significantly influenced by the geometry and density of the IGM (Gurung-López et al. 2019, 2020). This small-scale effect may obscure certain parts of structures, such as extremely overdense and dusty centers of some protoclusters, but it is unlikely to miss entire protoclusters, as seen in our maps. The photoz density map complements the LAE density map because the photoz-selected galaxies have a precision similar to that of the MQGs.

Our analysis shows that only 20% of our MQGs are located in protoclusters. The spatial distribution of quiescent galaxies relative to protocluster centers is similar to that of the general

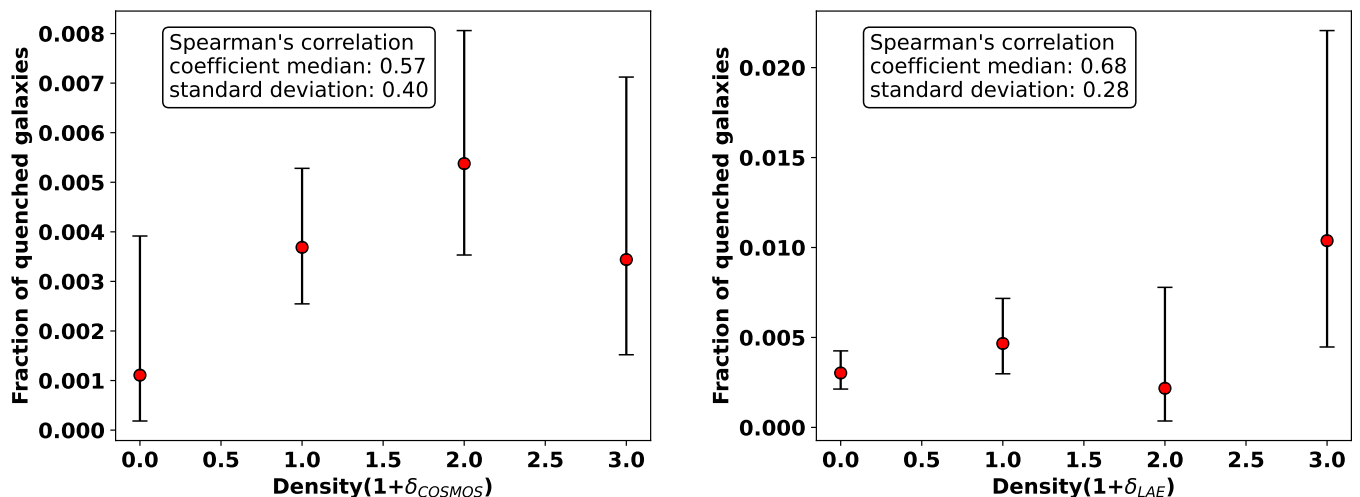


Fig. 8: Left: Evolution of the quenched fraction with the local density,  $\log(1+\delta)$  in the COSMOS2020 density map. Right: Evolution of the quenched fraction with the local density,  $\log(1+\delta)$  in the LAE density map.

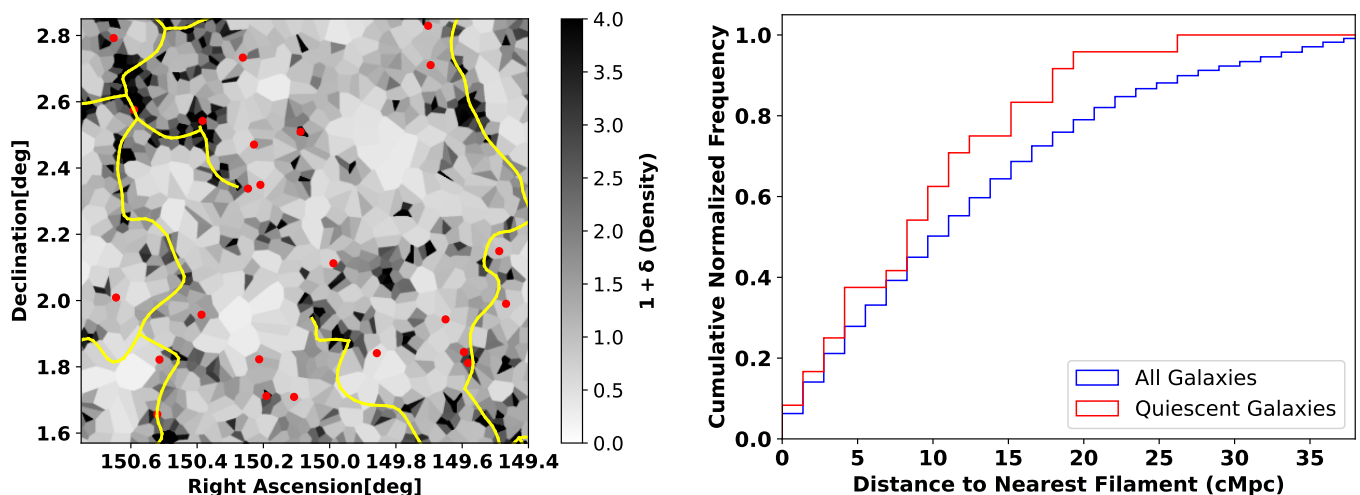


Fig. 9: Left: Filaments (yellow lines) discovered using DisPerSE by Ramakrishnan et al. (2023), overlaid on the LAE density map. The red points represent the MQGs. Right: Cumulative distribution of the distances to the nearest filaments for MQGs and all the photo-z selected galaxies.

galaxy population. Therefore, MQGs do not show a higher tendency to be found in protoclusters than other types of galaxies. As noted in Section 3.4, MQGs have a comparable number of neighbors within the entire range from 0.5 to 6 Mpc as the general galaxy population, i.e. they show a very similar environment. This suggests that environmental mechanisms prevalent in protoclusters or galaxy groups, such as ram pressure stripping, galaxy-galaxy interactions, strangulation, harassment, tidal stripping, and thermal evaporation, are not the sole factors responsible for quenching MQGs. Supporting this, studies using IllustrisTNG simulation have shown that environmental processes like mergers are not responsible for quenching galaxies at high redshift. Kurinchi-Vendhan et al. (2023) found that merger events do not significantly distinguish between quiescent and star-forming galaxies in the IllustrisTNG300 simulation and are unlikely to drive galaxy quenching at  $z>3$ . Their study concluded that quenched galaxies have experienced longer and more

intense AGN activity, releasing larger amounts of thermal energy than star-forming galaxies, prior to quenching.

We find that MQGs do not exhibit a correlation with local density peaks of environmental density, as illustrated in Figure 8. Peaks in local density are often associated with massive galaxies, elevated merger rates, high concentrations of cold gas, and increased AGN activity (Kauffmann et al. 2004; Allevato et al. 2011; Oman et al. 2013; Peng et al. 2010; Hopkins & Hernquist 2006). Our MQGs are massive, with stellar masses greater than  $10^{10.6}M_{\odot}$ . Given that massive galaxies are typically found in dense environments, the observed mild positive correlation with density may result from the local density peaks near these massive galaxies. Since high-density regions also serve as reservoirs of cold gas, mechanisms to heat the gas are necessary to prevent further accretion of cold gas and rejuvenation of star formation. In this context, AGN feedback is a plausible quenching mechanism.

AGN feedback is a secular quenching mechanism that can quench galaxies in a wide range of environments. AGN outflows cause the expulsion of gas from the gravitational bounds of their host galaxies, consequently reducing the subsequent star formation activity (DeBuhr et al. 2012; Combes 2017). Additionally, AGNs can heat the cool gas in the interstellar medium, further preventing the formation of new stars (Croton et al. 2006; Man & Belli 2018; Zinger et al. 2020). Recently, several observational studies using JWST and ALMA have found signs of gas outflows driven by AGN in massive quiescent galaxies at  $z > 3$  in morphological and spectroscopic observations (Kubo et al. 2022; Ito et al. 2022; Park et al. 2024; Pérez-González et al. 2024; Davies et al. 2024). Park et al. (2024); Glazebrook et al. (2024); D’Eugenio et al. (2023); Ito et al. (2022); Kubo et al. (2022) have found multiphase outflows and neutral gas outflows in massive quiescent galaxies along with evidence of AGN. Ito et al. (2022) find AGN activity ubiquitously in massive quiescent galaxies up to  $z = 5$ . In this context, quenching due to AGN feedback is consistent with our observation that MQGs are not correlated with protoclusters and have a similar number of neighbors as other types of galaxies.

In their study using the Magneticum simulation, Kimmig et al. (2023) also found that galaxies are quenched before cosmic noon ( $z = 3.42$ ) primarily because of the removal of gas by AGN feedback. However, Kimmig et al. (2023) predict the quenching process is also influenced by the environment. They showed that for a galaxy to be quenched, it must reside in a significant underdensity, preventing the replenishment of cold gas. In contrast to their study, we do not observe any preference for MQGs to reside in underdense regions. Instead, MQGs exhibit a random distribution with respect to protoclusters, suggesting that the effect of the environment may not be significant for quenching at a redshift of approximately 3.1.

Filaments traced by LAEs are reservoirs of neutral gas that can rejuvenate galaxies even if a starburst has consumed all of the gas. We do not observe any anticorrelation between the position of MQGs and filaments. In fact, 25% of our MQGs occur within 5cMpc of gas-rich filaments. This could be an indication of the action of physical processes that heat the gas near the galaxies, preventing the accretion of cold gas. This could further point to AGN heating the gas around the galaxies.

By performing SED fitting, we have obtained the star-formation history of our MQGs. It is typically characterized by a starburst phase, followed by a quenching period, with a timescale shorter than 500 Myr (Figure 3). The uniformity in the duration of quenching of these galaxies suggests that they were quenched by the same mechanism and physical processes which are unlikely strictly related to the environment. This quenching mechanism would include a massive starburst that consumes gas rapidly, along with a mechanism to prevent the inflow of cold gas to maintain star formation. A rapid quenching phase has been observed in other studies in the literature, such as Whitaker et al. (2012); Wild et al. (2016); Schreiber et al. (2018); Carnall et al. (2018); D’Eugenio et al. (2020); Carnall et al. (2023). Quenching timescales obtained from the simulations (e.g., Wright et al. 2019; Wetzel et al. 2013; Walters et al. 2022) can help to distinguish between the quenching mechanisms. In general, we can distinguish quenching between fast-quenching mechanisms ( $\sim 0.1$  Gyr) and slow-quenching ( $\sim 1$  Gyr) mechanisms. Furthermore, any trend in the quenching timescale with environment density can indicate the dependence of the quenching mechanism on the local environment. Environmental processes that are typically much slower are hence unlikely to quench these galaxies (Mao et al. 2022).

From Figure 6 we can see that the time it takes to quench a galaxy is not strongly correlated with the density of the local environment. A similar result is found in Figure 7 where we have shown the quenching timescale with respect to LAE densities. No correlation between quenching timescale and the environment indicates that the environment alone may not be the significant driver of quenching. Similarly, on the right panel of Figures 6 and 7 we can see that there exists no correlation between the  $SFR_{peak}$  and the environment density. We conclude that the SFH and hence the processes that quenched these MQGs do not have a strong dependence on the environment.

In order to spectroscopically confirm the redshift and obtain a more precise constraint on the star formation history (SFH) and stellar mass, acquiring spectra is essential. JWST *Nirspec* follow-up observations can be used to spectroscopically confirm MQGs at  $z \sim 3.1$ . Follow-up observations with the JWST *Nirspec* will be instrumental in identifying AGN-driven outflows as well as neutral gas outflows, which may play a role in quenching star formation. Furthermore, morphological analysis using NIR-Cam would provide valuable insight into the impact of mergers within dense environments.

## 5. Conclusions

In this study, we have investigated the quenching of massive quiescent galaxies in the early universe at redshifts  $z \approx 3.1$ , using data from the COSMOS2020 catalog and the ODIN survey. We employed Voronoi Monte Carlo mapping to characterize the galaxy environment and analyzed the relationship between quenching and environmental density using two independent tracers, namely Lyman- $\alpha$  emitters and the galaxies selected from the COSMOS2020 catalog.

Our key findings are summarized as follows:

- We identify 24 MQG candidates at  $3.004 < z < 3.224$  in the total surveyed volume in COSMOS of  $8.71 \times 10^5$  cMpc<sup>3</sup>. We calculate the number density of massive quiescent galaxies as  $2.87 \times 10^{-5}$  galaxies cMpc<sup>-3</sup> in agreement with the literature. All are massive with stellar masses  $> 10^{10.6} M_{\odot}$ .
- Using the BAGPIPES code, we have estimated the quenching timescales for MQGs. Our analysis reveals that the quenching period for MQGs is consistently short, generally less than 500 million years, and, in some cases, as brief as 100 million years. The star formation histories of these galaxies are notably similar, with an initial starburst phase followed by a rapid decline in star formation. The duration of quenching is uniform across all MQGs and does not depend on the environment. This consistent quenching timescale implies a common quenching mechanism that operates largely independently of environmental factors. Additionally, the peak star formation rate is also found to not depend on the environment.
- We have characterized the environment of the MQGs with two independent tracers, namely LAEs and the general galaxy population from the COSMOS2020 catalog. The differences in the two density maps are mainly due to the difference in redshift precision of the two tracers.
- We find a very weak to no correlation between the fraction of quenched galaxies and the local environmental density. This result is true both for the LAE map and the COSMOS2020 density map. We conclude that environmental processes are

not the dominant quenching mechanism for MQGs. In order to further investigate this, we compare the distribution of MQGs and the general galaxy population with respect to the protocluster centers. We could not find any evidence of MQGs following a distribution different from the general population. We also find the MQGs to have the same number of neighbors as all galaxies within radii ranging from 0.1 to 6 cMpc, further suggesting that they live in very similar environments. This indicates that quenching processes in protoclusters such as mergers, ram-pressure stripping, galaxy harassment, and interactions are not the dominant quenching mechanism at redshift=3.1.

Our results suggest that quenching mechanisms are likely driven by similar physical processes independent of their environments. Internal processes, such as AGN feedback, virial shocks, or morphological quenching, could possibly be more crucial in quenching at high redshifts than environmental factors such as galaxy mergers and interactions. The fact that the quiescent fraction does not decrease in a gas-rich environment (which includes filaments and high-density regions) indicates a gas-heating mechanism required to play. Environmental processes could contribute to quenching in the overdense regions but are not sufficient to explain quenching without gas-heating processes.

Future studies, including spectroscopic follow-ups with instruments such as JWST and ALMA, are therefore essential to understanding the detailed processes behind galaxy quenching. These observations will help constrain the star formation histories, ages, and metallicities of MQGs, providing deeper insights into their evolution and the role of internal and environmental factors in their quenching.

*Acknowledgements.* AS and LG acknowledge the FONDECYT regular project number 1230591 for financial support. EG and KSL acknowledge support from NSF grants AST-2206222, AST-2206705, and AST-2408359. Based on observations at Cerro Tololo Inter-American Observatory, NSF's NOIRLab (NOIRLab Prop. ID 2020B0201; PI: K.-S. Lee), which is managed by the Association of Universities for Research in Astronomy (AURA) under a cooperative agreement with the National Science Foundation.

## References

- Aihara, H., AlSayyad, Y., Ando, M., et al. 2019, *Publications of the Astronomical Society of Japan*, 71, 114
- Allevato, V., Finoguenov, A., Hasinger, G., et al. 2011, *The Astrophysical Journal*, 736, 99
- Arnouts, S., Cristiani, S., Moscardini, L., et al. 1999, *Monthly Notices of the Royal Astronomical Society*, 310, 540
- Barbary, K. 2016, *Journal of Open Source Software*, 1, 58
- Bertin, E. & Arnouts, S. 1996, *A&AS*, 117, 393
- Boselli, A., Fossati, M., & Sun, M. 2022, *The Astronomy and astrophysics review*, 30, 3
- Boselli, A. & Gavazzi, G. 2006, *PASP*, 118, 517
- Bressan, A., Marigo, P., Girardi, L., et al. 2012, *Monthly Notices of the Royal Astronomical Society*, 427, 127
- Bruzual, G. & Charlot, S. 2003, *Monthly Notices of the Royal Astronomical Society*, 344, 1000
- Calvi, R., Castignani, G., & Dannerbauer, H. 2023, *Astronomy & Astrophysics*, 678, A15
- Calzetti, D., Armus, L., Bohlin, R. C., et al. 2000, *The Astrophysical Journal*, 533, 682
- Carnall, A., McLeod, D., McLure, R., et al. 2023, *Monthly Notices of the Royal Astronomical Society*, 520, 3974
- Carnall, A. C., McLure, R. J., Dunlop, J. S., & Davé, R. 2018, *Monthly Notices of the Royal Astronomical Society*, 480, 4379–4401
- Casey, C. M. 2016, *The Astrophysical Journal*, 824, 36
- Ceverino, D. & Klypin, A. 2009, *The Astrophysical Journal*, 695, 292
- Chevallard, J. & Charlot, S. 2016, *Monthly Notices of the Royal Astronomical Society*, 462, 1415
- Cicone, C., Maiolino, R., Sturm, E., et al. 2014, *Astronomy & Astrophysics*, 562, A21
- Combes, F. 2017, *Frontiers in Astronomy and Space Sciences*, 4, 10
- Cowie, L. L. & Songaila, A. 1977, *nature*, 266, 501
- Croton, D. J., Springel, V., White, S. D., et al. 2006, *Monthly Notices of the Royal Astronomical Society*, 365, 11
- Cucciati, O., Lemaux, B., Zamorani, G., et al. 2018, *Astronomy & Astrophysics*, 619, A49
- Davé, R., Thompson, R., & Hopkins, P. F. 2016, *Monthly Notices of the Royal Astronomical Society*, 462, 3265
- Davies, R., Belli, S., Benton, C., et al. 2024, *Feedback and quenching: separating neutral gas in outflows and galaxies at z 2*, JWST Proposal. Cycle 3, ID. #5427
- DeBuhr, J., Quataert, E., & Ma, C.-P. 2012, *Monthly Notices of the Royal Astronomical Society*, 420, 2221
- D'Eugenio, F., Perez-Gonzalez, P., Maiolino, R., et al. 2023, *arXiv e-prints*, arXiv:2308.06317
- Dressler, A. 1980, *ApJ*, 236, 351
- Dunlop, J. S., Bowler, R. A., Franx, M., et al. 2023, *A Decade of ESO Wide-field Imaging Surveys (surveys2023)*, 10
- D'Eugenio, C., Daddi, E., Gobat, R., et al. 2020, *The Astrophysical Journal Letters*, 892, L2
- Fabian, A. C. 2012, *Annual Review of Astronomy and Astrophysics*, 50, 455
- Falcón-Barroso, J., Sánchez-Blázquez, P., Vazdekis, A., et al. 2011, *Astronomy & Astrophysics*, 532, A95
- Firestone, N. M., Gawiser, E., Ramakrishnan, V., et al. 2023, *ODIN: Improved Narrowband Ly $\alpha$  Emitter Selection Techniques for z = 2.4, 3.1, and 4.5*
- Forrest, B., Annunziatella, M., Wilson, G., et al. 2020, *The Astrophysical Journal Letters*, 890, L1
- Forrest, B., Lemaux, B. C., Shah, E., et al. 2023, *arXiv preprint arXiv:2307.15113*
- Gawiser, E., Francke, H., Lai, K., et al. 2007, *The Astrophysical Journal*, 671, 278
- Gehrels, N. 1986, *ApJ*, 303, 336
- Girelli, G., Bolzonella, M., & Cimatti, A. 2019, *A&A*, 632, A80
- Glazebrook, K., Nanayakkara, T., Marchesini, D., Kacprzak, G., & Jacobs, C. 2022, *Proceedings of the International Astronomical Union*, 18, 3
- Glazebrook, K., Nanayakkara, T., Marchesini, D., Kacprzak, G., & Jacobs, C. 2024, in *Early Disk-Galaxy Formation from JWST to the Milky Way*, ed. F. Tabatabaei, B. Barbuy, & Y.-S. Ting, Vol. 377, 3–8
- Glazebrook, K., Schreiber, C., Labbé, I., et al. 2017, *Nature*, 544, 71
- Gunn, J. E. & Gott III, J. R. 1972, *Astrophysical Journal*, vol. 176, p. 1, 176, 1
- Gurung-López, S., Orsi, Á. A., Bonoli, S., Baugh, C. M., & Lacey, C. G. 2019, *MNRAS*, 486, 1882
- Gurung-López, S., Orsi, Á. A., Bonoli, S., et al. 2020, *MNRAS*, 491, 3266
- Hartley, A. I., Nelson, E. J., Suess, K. A., et al. 2023, *Monthly Notices of the Royal Astronomical Society*, 522, 3138
- Hopkins, P. F. & Hernquist, L. 2006, *The Astrophysical Journal Supplement Series*, 166, 1
- Hu, E. M. & McMahon, R. G. 1996, *Nature*, 382, 231
- Hung, D., Lemaux, B., Gal, R., et al. 2020, *Monthly Notices of the Royal Astronomical Society*, 491, 5524
- Ito, K., Tanaka, M., Miyaji, T., et al. 2022, *ApJ*, 929, 53
- Ito, K., Tanaka, M., Valentino, F., et al. 2023, *The Astrophysical Journal Letters*, 945, L9
- Ito, K., Tanaka, M., Valentino, F., et al. 2023, *ApJ*, 945, L9
- Jin, S., Sillassen, N. B., Magdis, G. E., et al. 2024, *Astronomy & Astrophysics*, 683, L4
- Kauffmann, G. et al. 2004, *Monthly Notices of the Royal Astronomical Society*, 353, 713
- Kimmig, L. C., Remus, R.-S., Seidel, B., et al. 2023, *arXiv preprint arXiv:2310.16085*
- Kovač, K., Somerville, R. S., Rhoads, J. E., Malhotra, S., & Wang, J. 2007, *The Astrophysical Journal*, 668, 15
- Kubo, M., Umehata, H., Matsuda, Y., et al. 2022, *ApJ*, 935, 89
- Kurinchi-Vendhan, S., Farcy, M., Hirschmann, M., & Valentino, F. 2023, *arXiv preprint arXiv:2310.03083*
- Larson, R. B. 1990, *Publications of the Astronomical Society of the Pacific*, 102, 709
- Le Fèvre, O., Cassata, P., Cucciati, O., et al. 2013, *Astronomy & Astrophysics*, 559, A14
- Lee, K.-S., Gawiser, E., Park, C., et al. 2024, *ApJ*, 962, 36
- Lemaux, B., Cucciati, O., Tasca, L., et al. 2014, *Astronomy & Astrophysics*, 572, A41
- Lemaux, B. C., Le Fèvre, O., Cucciati, O., et al. 2018, *Astronomy & astrophysics*, 615, A77
- Man, A. & Belli, S. 2018, *Nature Astronomy*, 2, 695

- Mao, Z., Kodama, T., Pérez-Martínez, J. M., et al. 2022, *Astronomy & Astrophysics*, 666, A141
- Marigo, P., Girardi, L., Bressan, A., et al. 2017, *The Astrophysical Journal*, 835, 77
- McCracken, H., Milvang-Jensen, B., Dunlop, J., et al. 2012, *Astronomy & Astrophysics*, 544, A156
- Merlin, E., Fortuni, F., Torelli, M., et al. 2019, *Monthly Notices of the Royal Astronomical Society*, 490, 3309
- Moore, B., Katz, N., Lake, G., Dressler, A., & Oemler, A. 1996, *nature*, 379, 613
- Nanayakkara, T., Glazebrook, K., Jacobs, C., et al. 2024, *Scientific Reports*, 14, 3724
- Oman, K. A. et al. 2013, *Monthly Notices of the Royal Astronomical Society*, 431, 230
- Ouchi, M., Ono, Y., & Shibuya, T. 2020, *Annual Review of Astronomy and Astrophysics*, 58, 617
- Ouchi, M., Shimasaku, K., Furusawa, H., et al. 2003, *The Astrophysical Journal*, 582, 60
- Pacifici, C., Oh, S., Oh, K., Lee, J., & Suhyoung, K. Y. 2016, *The Astrophysical Journal*, 824, 45
- Park, C. & Hwang, H. S. 2009, *ApJ*, 699, 1595
- Park, M., Belli, S., Conroy, C., et al. 2024, arXiv e-prints, arXiv:2404.17945
- Peng, Y. et al. 2010, *The Astrophysical Journal*, 721, 193
- Pérez-González, P. G., D'Eugenio, F., Rodríguez del Pino, B., et al. 2024, arXiv e-prints, arXiv:2405.03744
- Ramakrishnan, V., Moon, B., Im, S. H., et al. 2023, *The Astrophysical Journal*, 951, 119
- Rodríguez Montero, F., Davé, R., Wild, V., Anglés-Alcázar, D., & Narayanan, D. 2019, *Monthly Notices of the Royal Astronomical Society*, 490, 2139
- Salim, S. & Narayanan, D. 2020, *Annual Review of Astronomy and Astrophysics*, 58, 529
- Sanchez-Blazquez, P., Peletier, R., Jimenez-Vicente, J., et al. 2006, *Monthly Notices of the Royal Astronomical Society*, 371, 703
- Schreiber, C., Glazebrook, K., Nanayakkara, T., et al. 2018, *Astronomy & Astrophysics*, 618, A85
- Scoville, N., Aussel, H., Brusa, M., et al. 2007, *The Astrophysical Journal Supplement Series*, 172, 1
- Shah, E. A., Lemaux, B., Forrest, B., et al. 2024, *Monthly Notices of the Royal Astronomical Society*, stae519
- Sousbie, T. 2011, *Monthly notices of the royal astronomical society*, 414, 350
- Spitler, L. R., Straatman, C. M., Labbé, I., et al. 2014, *The Astrophysical Journal Letters*, 787, L36
- Straatman, C. M., Labbé, I., Spitler, L. R., et al. 2014, *The Astrophysical Journal Letters*, 783, L14
- Tanaka, M., Onodera, M., Shimakawa, R., et al. 2024, *The Astrophysical Journal*, 970, 59
- Valentino, F., Tanaka, M., Davidzon, I., et al. 2020, *The Astrophysical Journal*, 889, 93
- Walters, D., Woo, J., & Ellison, S. L. 2022, *Monthly Notices of the Royal Astronomical Society*, 511, 6126
- Weaver, J. R., Kauffmann, O., Shuntov, M., et al. 2021, in *American Astronomical Society Meeting Abstracts*, Vol. 53, American Astronomical Society Meeting Abstracts, 215.06
- Wetzel, A. R., Tinker, J. L., Conroy, C., & Van Den Bosch, F. C. 2013, *Monthly Notices of the Royal Astronomical Society*, 432, 336
- Whitaker, K. E., Kriek, M., van Dokkum, P. G., et al. 2012, *The Astrophysical Journal*, 745, 179
- Wild, V., Almaini, O., Dunlop, J., et al. 2016, *Monthly Notices of the Royal Astronomical Society*, 463, 832
- Williams, R. J., Quadri, R. F., Franx, M., van Dokkum, P., & Labbé, I. 2009, *ApJ*, 691, 1879
- Wright, R. J., Lagos, C. d. P., Davies, L. J., et al. 2019, *Monthly Notices of the Royal Astronomical Society*, 487, 3740
- Zinger, E., Pillepich, A., Nelson, D., et al. 2020, *Monthly Notices of the Royal Astronomical Society*, 499, 768



## Appendix A: Simulations to check the validity of correlation

In Figure 8, we plot the quenched fraction versus the local density on the COSMOS2020 and LAE maps. The distributions are correlated with the density, which is visually apparent and confirmed by the Spearman correlation coefficient test. This suggests that the location of quiescent galaxies depends on the local environment density. This observation might seem surprising because high-density regions have high amounts of cold gas that could replenish the star formation in galaxies. We performed a test to investigate whether our current data are sufficient to detect the presence (or absence) of a correlation between the quenched fraction and the local density.

To quantify the discriminating power of our dataset, we select galaxies and designate them as ‘MQGs’. We select 6 sets of galaxies, each containing 25, 50, 100, 200, 250, and 300 galaxies, respectively. These galaxies are not selected entirely randomly. We first select sets with a “strong correlation” with the local density. They are selected such that:

- 70 % of the set lies in highly overdense regions ( $\delta > 3$ )
- 20 % of the set lies in overdense region ( $2 < \delta < 3$ )
- 5 % of the set lies in average density region ( $1 < \delta < 2$ )
- 5 % of the set lies in underdense region ( $\delta < 1$ )

From this simulation, we conclude that if a strong correlation existed, we would be able to find it using our analysis, even with a relatively small sample of 24 galaxies. However, for a smaller sample of galaxies (up to 100), the Spearman correlation coefficient is overestimated and finally converges for 150 or more sources. The mean correlation coefficient calculated for our sample in Section 3.3 is 0.55 and therefore we can confidently rule out the presence of a strong correlation between the quenched fraction and the environmental density.

Using these mock samples, we repeat the analysis steps from Sections 3.3 to measure the quenched fraction and the Spearman coefficient. In the strongly correlated sample, we can see that the Spearman correlation coefficient is observed to be  $\approx 1$ , even for a small sample of 25 galaxies. The correlation coefficient does not become stronger on increasing the number of selected galaxies.

We repeat this analysis for a weakly correlated sample generated such that:

- 15 % of the set lies in highly overdense regions ( $\delta > 3$ )
- 20 % of the set lies in overdense region ( $2 < \delta < 3$ )
- 45 % of the set lies in average density region ( $1 < \delta < 2$ )
- 20 % of the set lies in underdense region ( $\delta < 1$ )

In this weakly correlated sample, we can also see a correlation at a median  $\approx 0.6$ . The Spearman correlation coefficient increases with an increase in the number of selected sources. From these simulations, we conclude that if a correlation existed, we would be able to find it using our analysis, even with a relatively small sample of 24 galaxies, as in the main part of this paper. Further notable is that even for a small number of sources, no more than 22% of the Monte Carlo runs show no correlation ( $SC < 0.4$ ). In this case too, for a small number of sources, the correlation coefficient can be overestimated, with nearly 50% of the Monte Carlo predictions incorrectly showing a strong correlation. This is different from our calculations in Section 3.3 where nearly 45% of Monte Carlo, where  $SC < 0.4$ . We conclude from this that there exists a weak to no correlation between quenched fraction and the environment density.

Number of "MQGs"	mean SC	standard deviation SC	$f_{SC < 0.4}$	$f_{SC \geq 0.7}$
25	0.87	0.15	5.6	94.4
50	0.86	0.10	0.67	99.33
75	0.84	0.08	0.0	100.0
100	0.81	0.04	0.0	100.0
150	0.80	0.11e-16	0.0	100.0
200	0.80	0.11e-16	0.0	100.0
250	0.80	0.11e-16	0.0	100.0
300	0.80	0.11e-16	0.0	100.0

Table A.1: The statistics obtained for the strongly correlated simulated sample. Columns 2 and 3 display the mean and standard deviation of the 3,000 Spearman coefficient (SC) Monte Carlo runs. Columns 4 and 5 show the fraction as percentage when the SC is  $< 0.4$  and the SC is  $> 0.7$  respectively.

Number of "MQGs"	mean SC	standard deviation SC	$f_{SC < 0.4}$	$f_{SC \geq 0.7}$
25	0.586	0.357	21.9	49.3
50	0.553	0.283	17.9	29.5
75	0.564	0.259	14.9	27.4
100	0.558	0.232	13.3	18.9
150	0.601	0.165	5.6	17.5
200	0.614	0.127	2.8	15.3
250	0.614	0.094	1.3	11.1
300	0.610	0.082	1.0	8.1

Table A.2: The statistics obtained for weakly correlated samples. Columns 2 and 3 display the mean and standard deviation of the 3000 Spearman coefficient (SC) Monte Carlo runs. Columns 4 and 5 show the percentage of runs in which the SC is  $< 0.4$  and  $> 0.7$ , respectively.

## **Appendix A: SEDs of selected MQGs**

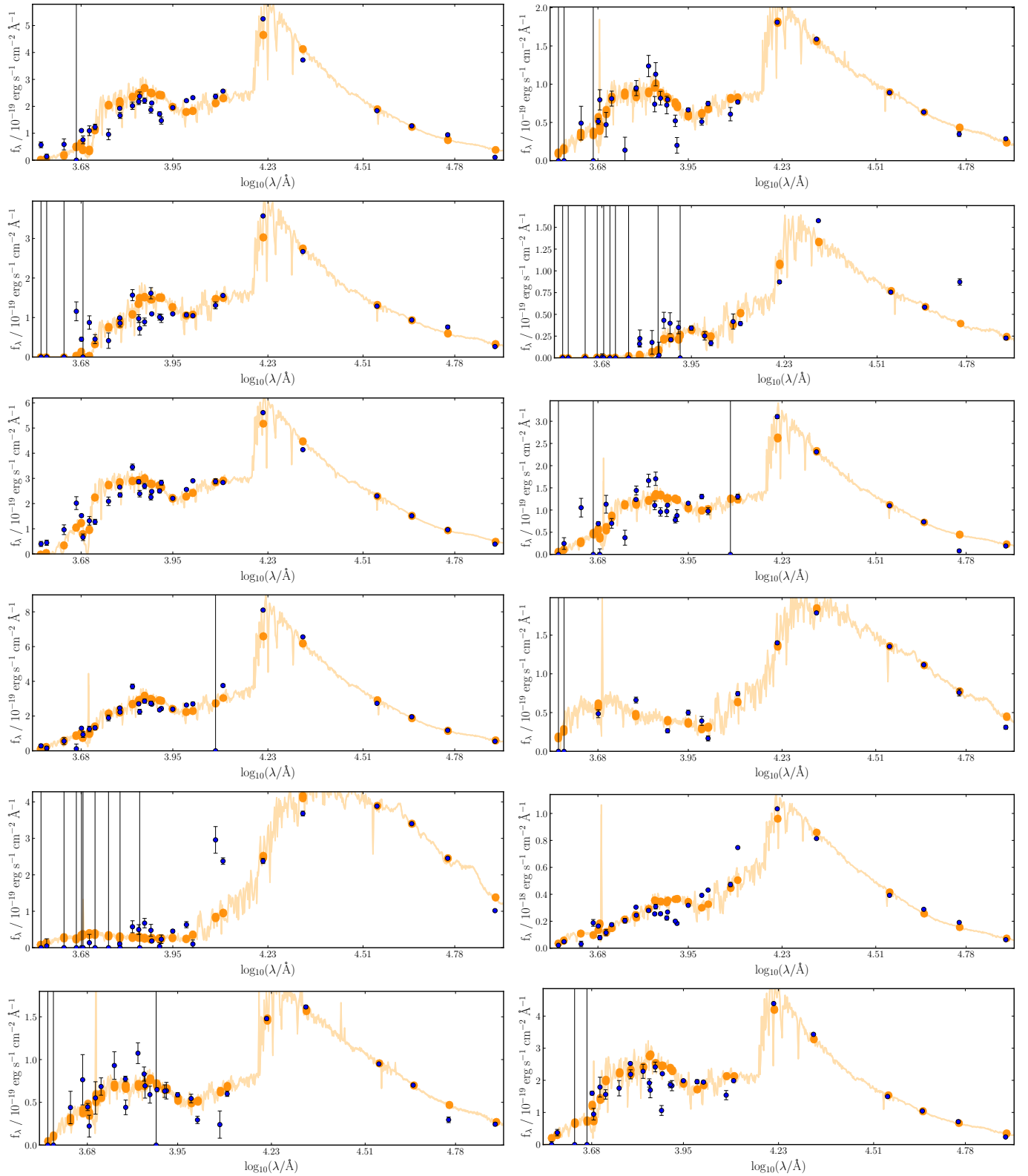


Fig. A.1: SED fitting of massive quiescent galaxies obtained with the BAGPIPES code and using the double power law star formation history model. The blue points with error bars represent the input photometry from the COSMOS2020 catalog. The 16<sup>th</sup> to 84<sup>th</sup> percentile range for the posterior spectrum and photometry are shaded orange lines. The orange points correspond to the models convolved with the photometric band filters. The black lines are error bars for bands where flux is either not available, or there was a non-detection. Following the prescription in the BAGPIPES code documentation we have assigned a large value ( $\approx 10^{100}$ ) to such bands.

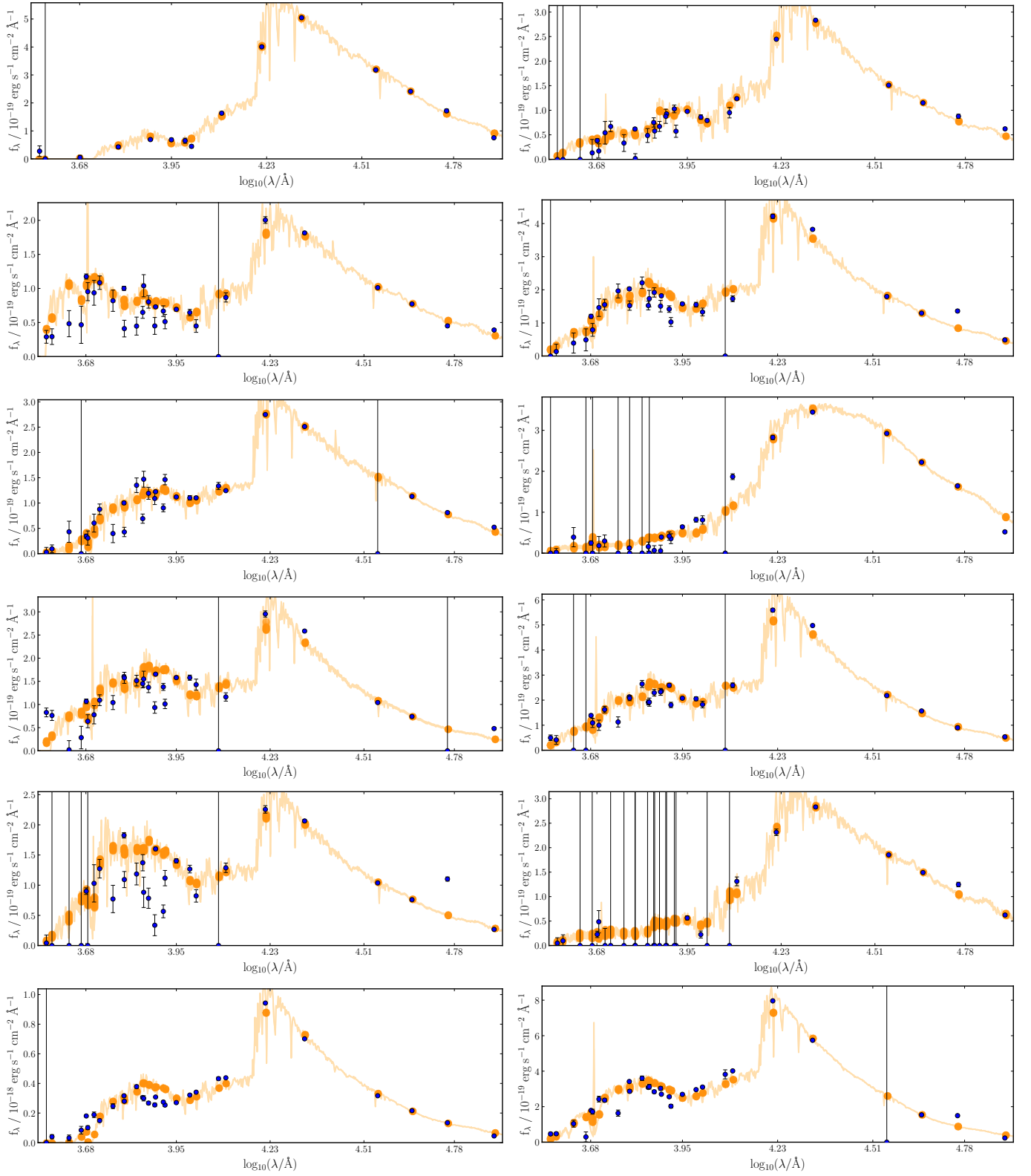


Fig. A.2: SED fitting of massive quiescent galaxies obtained with the BAGPIPES code and using the double power law star formation history model. The blue points with error bars represent the input photometry from the COSMOS2020 catalog. The 16<sup>th</sup> to 84<sup>th</sup> percentile ranges for the posterior spectrum and photometry are shaded orange lines. The orange points correspond to the models convolved with the photometric band filters. The black lines are error bars for bands where the flux is either not available, or there was a non-detection. Following the prescription in the BAGPIPES code documentation, we have assigned a large value ( $\approx 10^{100}$ ) to such bands.



## Appendix A: Visual Inspection of Galaxies

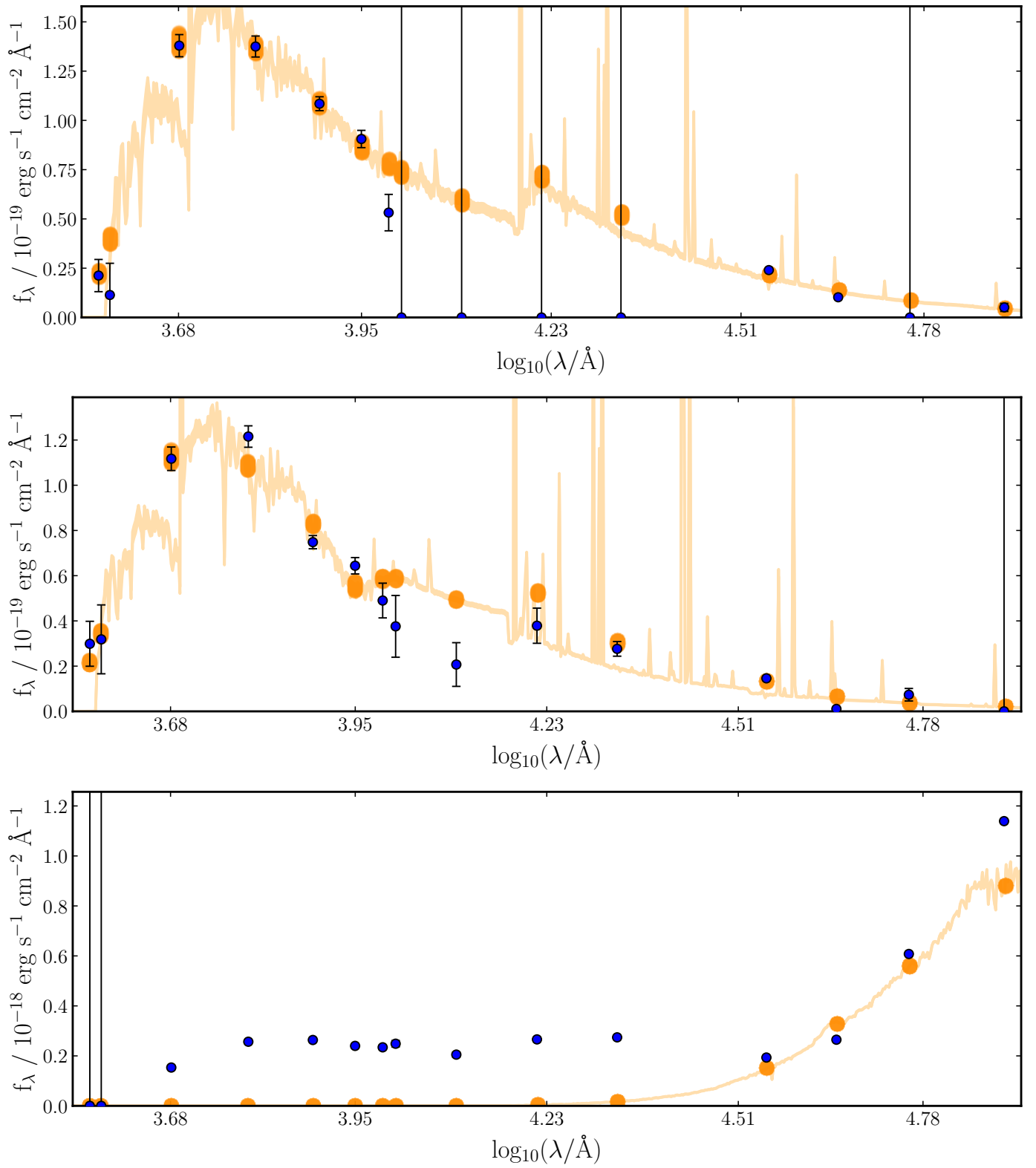


Fig. A.1: Examples of galaxies rejected from the MQG sample after visual inspection.

## Appendix A: Nearest Neighbors

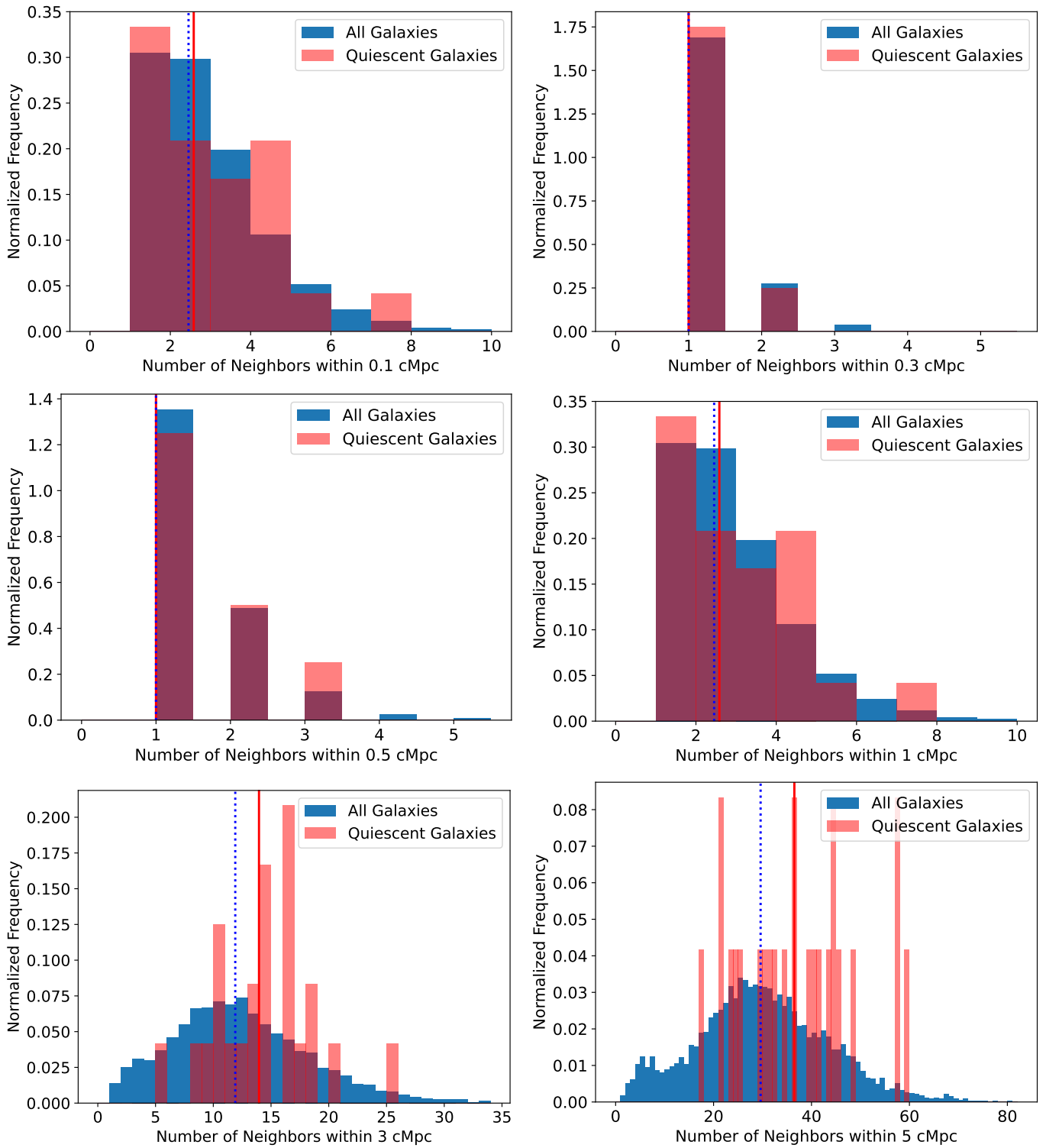


Fig. A.1: Number of neighbors within radii of 0.1-6 Mpc for all galaxies and MQGs. The vertical line represents the mean of the distributions.